

Article

The Effects of Functional Groups and Missing Linkers on the Adsorption Capacity of Aromatic Hydrocarbons in UiO-66 Thin Films

Jennifer Shankwitz ¹, Daniel Speed ¹, Dillon Sinanan ² and Greg Szulczewski ^{1,*}

¹ Department of Chemistry and Biochemistry, The University of Alabama, Tuscaloosa, AL 35487, USA; jeshankwitz@crimson.ua.edu (J.S.); dspeed@crimson.ua.edu (D.S.)

² Department of Biological and Chemical Engineering, The University of Alabama, Tuscaloosa, AL 35487, USA; djsinanan@crimson.ua.edu

* Correspondence: gjs@ua.edu; Tel.: +1-205-348-8428

Abstract: The adsorption of benzene, toluene, ethylbenzene, and xylene isomers, also known as BTEX, from the gas phase into porous thin films of the metal–organic framework UiO-66-X, where X = H, NH₂, and NO₂, was measured to quantify adsorption capacity. The thin films were grown by a vapor-conversion method onto Au-coated quartz microbalance crystals. The MOF thin films were characterized by IR and Raman spectroscopy, X-ray diffraction, X-ray photoelectron spectroscopy and scanning electron microscopy. The thin films were activated by heating under high vacuum and exposed to each gas to calculate the Henry’s constant. The results demonstrate that the functional groups in the organic linker and missing-linkers both play important roles in the adsorption capacity. Several trends can be observed in the data. First, all the compounds in the BTEX family have lower Henry’s constants in the UiO-66-H films compared to the UiO-66-NH₂ and UiO-66-NO₂ films, which can largely be attributed to the absence of a functional group on the linker. Second, at 25 °C, the Henry’s constants for all the BTEX compounds in UiO-66-NO₂ films are larger than UiO-66-NH₂ films. Third, the role of missing linkers is addressed by comparing the measured adsorption capacity to ideal pore filling. The results show that the UiO-66-H films are the most defect-free and the UiO-66-NO₂ films have the most missing linker defects.

Keywords: BTEX adsorption; Henry’s constant; metal–organic framework; thin films



Citation: Shankwitz, J.; Speed, D.; Sinanan, D.; Szulczewski, G. The Effects of Functional Groups and Missing Linkers on the Adsorption Capacity of Aromatic Hydrocarbons in UiO-66 Thin Films. *Inorganics* **2021**, *9*, 1. <https://doi.org/10.3390/inorganics9010001>

Received: 26 November 2020

Accepted: 21 December 2020

Published: 26 December 2020

Publisher’s Note: MDPI stays neutral with regard to jurisdictional claims in published maps and institutional affiliations.



Copyright: © 2020 by the authors. Licensee MDPI, Basel, Switzerland. This article is an open access article distributed under the terms and conditions of the Creative Commons Attribution (CC BY) license (<https://creativecommons.org/licenses/by/4.0/>).

1. Introduction

Metal–organic frameworks, or MOFs, have been widely studied over the past 20 years for possible applications in gas storage, separation, and sensors [1]. The modular nature of the synthesis has produced more than 50,000 structures, since a wide range of inorganic cations (“nodes”) and organic ligands can be combined together [2]. The appropriate choice of the chemical building blocks affords a porous three-dimensional solid that exhibits extremely high surface area. However, the pores are often filled by the solvent after the synthesis and must be removed for the applications mentioned above. In addition, the mechanical stability is often limited after the solvent is removed from the porous solid. In 2008 a significant advance in MOF synthesis was reported by Lillerud and co-workers at the University of Oslo [3]. Cavka et al. reported the first synthesis of UiO-66-H using 1,4-benzenedicarboxylic acid as the organic linker and Zr clusters as the inorganic “nodes” [3]. The material is stable over a large pH range in solution and showed excellent thermal stability [4–6]. The ideal structure of a UiO-66 unit-cell consists of a zirconium-oxo cluster, Zr₆O₄(OH)₄, to form a node and six terephthalic acid linkers. In the ideal UiO-66 framework, each Zr ion takes the vertex in an octahedron with the μ₃-O (triply bridging oxygen) and μ₃-OH groups forming the eight faces [7,8]. The external coordination spheres of the zirconium ions are formed by carboxylate donors forming the twelve edges of the

octahedron. In this way, the overall metal–organic framework forms as twelve clusters connected by terephthalic acid linkers to each other into a face-centered cubic array (fcu). As the nodes occupy corner and face sites of the fcu-type unit cell, the linkers will divide the cell into two types of pores, which are common in fcu-type frameworks. A single large central octahedral pore (~ 11 Å) in the center of the unit cell is formed by the space between the six facial nodes. Smaller tetrahedral pores (~ 8 Å) are then formed around the central pore by the linkers between three facial and one corner node, one for each corner of the cube. There are smaller triangular windows (~ 6 Å) that connect the two pores. The effective size of the triangular window is temperature dependent because the linker can rotate [9]. Otherwise, molecules with kinetic diameters larger than the window would not be able to pass through the framework.

The fundamental adsorption, desorption and diffusion processes of hydrocarbons into MOFs has been studied because of their industrial importance [10–20]. In particular, the separation of the BTEX family of compounds is very challenging due to the similar physical properties. Industrially the separation is accomplished with a simulated moving bed using zeolites. An interesting observation was discovered by Barcia et al. when they performed breakthrough measurements with ethylbenzene and xylene isomers on UiO-66-H pellets [21]. At 398 K and 423 K, *o*-xylene was retained longer than *p*-xylene from a mixture of vapors containing equal concentration. This result revealed a “reverse shape selectivity” phenomena, which states that the more bulky molecule is retained in favor the least bulky molecule. After this initial finding, others observed the reverse-shape selectivity phenomena for xylene isomers in gas and liquid chromatography experiments. For example, Chang and Yan used UiO-66-H as a stationary phase in capillary columns to separate a mixture xylene isomers and ethylbenzene [22]. They found that *p*-xylene eluted first, followed by *m*-xylene, ethylbenzene, and *o*-xylene, and calculated the adsorption enthalpy and entropy from the chromatograms. Subsequently, Duerinck et al. used inverse pulse gas chromatography to calculate the Henrys constants for BTEX compounds on a packed gas chromatography column of UiO-66-X where X was –H, –NO₂, and –CH₃ groups [14]. In general, they found that decreasing the pore diameter had the largest influence on adsorption properties, rather than the specific nature of the functional group.

In addition to the experimental work, some theoretical studies have been done to better understand the reverse shape selectivity. The first attempt to theoretically study the adsorption of xylene isomers in UiO-66-H was performed by Granato et al. using grand-canonical Monte Carlo simulations [23]. They used four different force fields (all models assumed a rigid UiO-66-H structure) to predict isotherms at 423 K for ethylbenzene and the xylene isomer. In general, the simulations confirmed the experimental ortho isomer selectivity. Subsequently, molecular dynamics simulations by Lennox and Düren were aimed at better understanding the diffusion mechanism of xylene isomers in UiO-66-H [9]. They found that rotation of the benzene dicarboxylate linker was crucial to allow passage of xylene isomers from pore to pore.

In this work, static vapor-phase adsorption of BTEX compounds into UiO-66-X thin films was studied to better understand the effect of functional groups on the adsorption of aromatic compounds. Our experimental approach is different than the previous breakthrough measurements and chromatographic studies in two ways. First, we measure the adsorption of a single compound to the MOF and second, there is no competitive adsorption from a non-adsorbing solvent. In addition, this is the first time UiO-66-NH₂ has been evaluated as a sorbent for BTEX. Lastly, by performing measurements near room temperature we are able to reach saturation adsorption capacity, which reveals insight about the role of missing linker defects.

2. Results and Discussion

X-ray diffraction was used to assess the crystallinity of the UiO-66 thin films. Figure 1 shows the low angle Bragg peaks for the thin films. The most intense peak near 7.5° corresponds to the (111) plane. A weaker reflection near 8.5° is due to the (200) plane.

In the UiO-66-H film, the (111) peak is the most intense and narrow peak, which indicates better crystallinity. In contrast, in the UiO-66-NO₂ film the (111) peak intensity is weaker and broader, which indicates less crystallinity. Previous work has shown the ratio of the intensity of the (111)/(200) peaks is a measure of missing linker defects [24]. The higher the intensity of the ratio of the (111)/(200) peaks, the fewer missing linkers. Consequently, the data in Figure 1 suggest that the UiO-66-H films have the fewest missing linkers and the UiO-66-NO₂ films have more missing linkers. Scanning electron microscopy was used to investigate the morphology and thickness of the films.

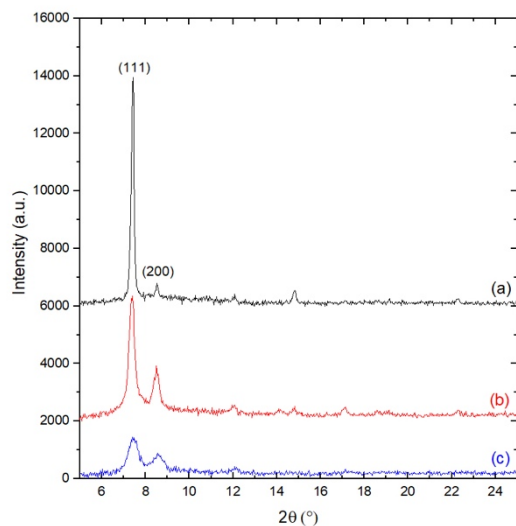


Figure 1. X-ray diffraction patterns of (a) UiO-66-H, (b) UiO-66-NH₂ and (c) UiO-66-NO₂ films.

Figure 2 shows SEM images of the top view of the UiO-66-X films. In general, each film is continuous with evidence of grain boundaries. There are some regions (not shown) where microscopic cracks are observed, which are attributed to stress while drying. Cross-section SEM images reveal the films are about 1–2 μm thick.

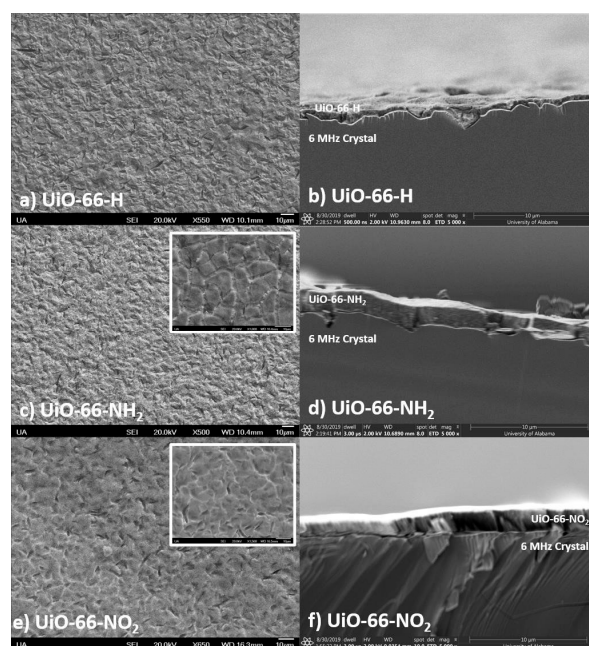


Figure 2. SEM images of UiO-66 films on QCM substrates. (a) Plane-view and (b) cross-sectional view of UiO-66-H. (c) Plane-view and (d) cross-sectional view of UiO-66-NH₂. (e) Plane-view and (f) cross-sectional view of UiO-66-NO₂.

Figure 3 shows IR spectra in the fingerprint region of the synthesized UiO-66-H, UiO-66-NH₂, and UiO-66-NO₂ films. The spectra are consistent with reports in literature for bulk powders [4,19]. There is a small peak around 1705–1655 cm⁻¹ that can be assigned to the carbonyl group of residual DMF solvent in the pores (which is removed upon activation before the adsorption studies). In all three RAIRS spectra, there are a set of strong peaks between 1580 and 1395 cm⁻¹ due to the symmetric and asymmetric carboxylate modes. There is also a strong C–H bending mode near 770 cm⁻¹ in all three films. There are several peaks unique to the amino and nitro functional groups. For example, in the UiO-66-NH₂ spectrum, the peaks at 1627 cm⁻¹ and 1260 cm⁻¹ are associated with the –NH₂ bending mode and C–N stretching of the amino group. In the case of the UiO-66-NO₂ spectrum, the peaks at 1540 cm⁻¹ and 1346 cm⁻¹ can be assigned to the asymmetric and symmetric stretching modes of the NO₂ group.

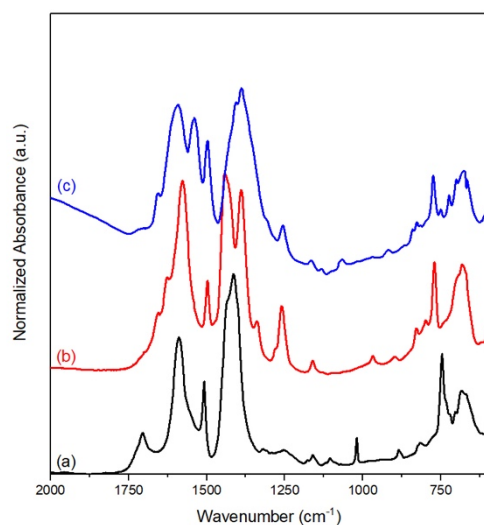


Figure 3. RAIRS of (a) UiO-66-H, (b) UiO-66-NH₂ and (c) UiO-66-NO₂ films.

Figure 4 shows the Raman spectra from 650 to 1800 cm⁻¹. In the spectrum for UiO-66-H, there are several strong peaks: (i) the peak at 1615 cm⁻¹ can be assigned to the carbon-carbon bond stretching mode of the aromatic ring of the linker, (ii) at peaks at 1450 cm⁻¹ and 1430 cm⁻¹ are two modes associated with the in-phase carboxylate stretching normal mode, (iii) the peak at 1145 cm⁻¹ can be assigned to the breathing mode of the terephthalate ring and (iv) and a peak at 860 cm⁻¹ due to a C–H in-plane bending mode of the linker. In the UiO-66-NO₂ Raman spectrum, there is an additional peak at 1351 cm⁻¹ assigned to the symmetric stretching mode of the –NO₂ group, and, in the UiO-66-NH₂ film, there is a new peak at 1265 cm⁻¹ that can be assigned to the –NH₂ bending mode.

Figure 5 shows survey X-ray photoelectron spectra. The main peaks for the MOF nodes are the O(1s), Zr(3d) and Zr(3p) peaks as seen near 520 eV, 183 eV and 330 eV, respectively. The main peak for the linker is the C(1s) at 285 eV. The N(1s) binding energy for the NH₂ and NO₂ groups are observed at 404 and 400 eV, respectively. There is a small Au(4f) peak seen in the UiO-66-NO₂ spectrum, which is from the substrate. The absence of Cl suggests there is no unreacted starting material.

Figure 6 shows a representative set of QCM data on a UiO-66-NH₂ film. Similar data sets for the UiO-66-H and UiO-66-NO₂ films are shown in the Supporting Information. In each experiment, the crystal frequency was recorded at each temperature until it stabilized. Multiple runs were measured after baking the chamber. The results of the multiple runs were averaged and used to calculate the Henry's constant at each temperature (Table S1 in Supplementary Materials). There are two global trends worth noting. First, the Henry's constants on the UiO-66-H are an order of magnitude smaller than the other two MOF films. Second, the Henry's constants for the UiO-66-NO₂ are greater than UiO-66-NH₂.

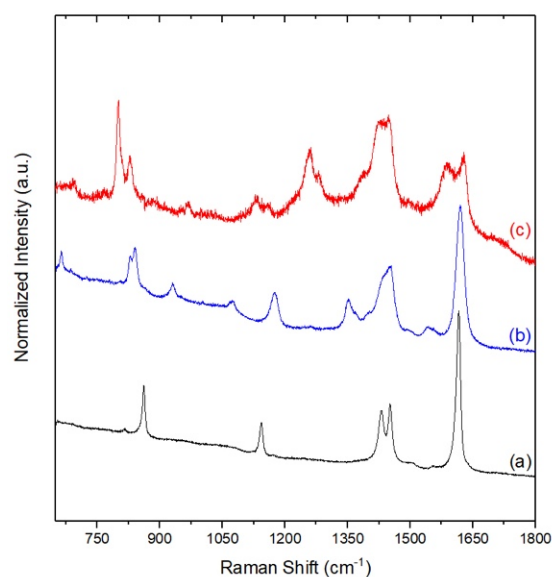


Figure 4. Raman spectra of (a) UiO-66-H, (b) UiO-66-NO₂ and (c) UiO-66-NH₂ films.

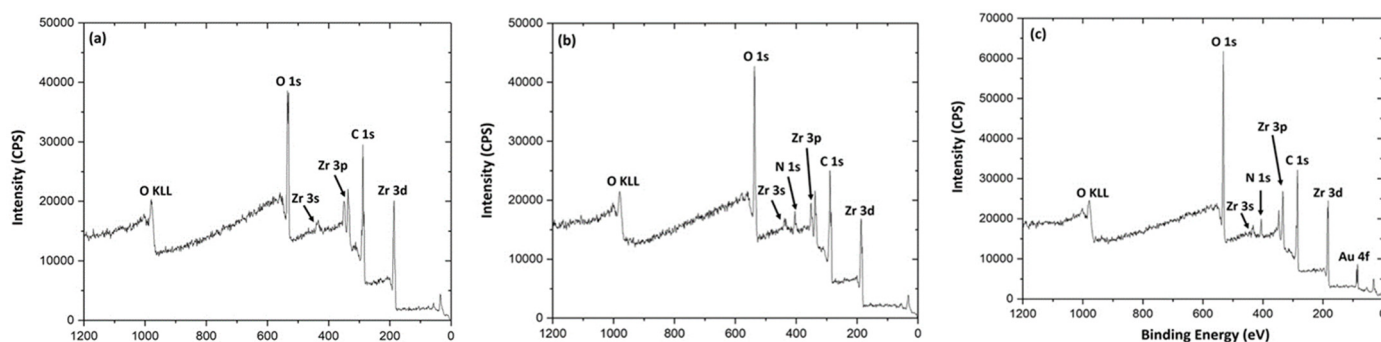


Figure 5. X-ray photoelectron spectra of (a) UiO-66-H, (b) UiO-66-NH₂ and (c) UiO-66-NO₂ films.

Our results indicate that larger substituents on the organic linker decrease the pore size and increase the interaction between the molecules and MOF framework. Previous nitrogen adsorption isotherms on UiO-66-X have shown a direct correlation between the functional group and the pore volume and surface area [4]. For example, in UiO-66-H the surface area has been measured to be near 1300 m²/g. In UiO-66-NH₂, the surface area decreases to 1250 m²/g. When the amine is replaced by a nitro group in UiO-66-NO₂, the surface area decreases to 856 m²/g. The porosity of the framework is sensitive to the synthesis conditions. In fact, the porosity can be tuned by the addition of monocarboxylic acids that act as modulators of the crystallization process [25–27]. The monocarboxylic acids compete with binding to the nodes, which slows the crystallization kinetics and can increase the crystallite size. In addition, the monocarboxylic acid promotes the formation of missing linker defects. It is well-established that using a stronger monocarboxylic acid in the synthesis increases the surface area [25]. The increase in surface area can be attributed to either missing linkers or missing nodes. It is very challenging to provide direct evidence for the missing linker defects. Initial work using thermal gravimetric analysis inferred the missing linkers based on stoichiometry arguments.

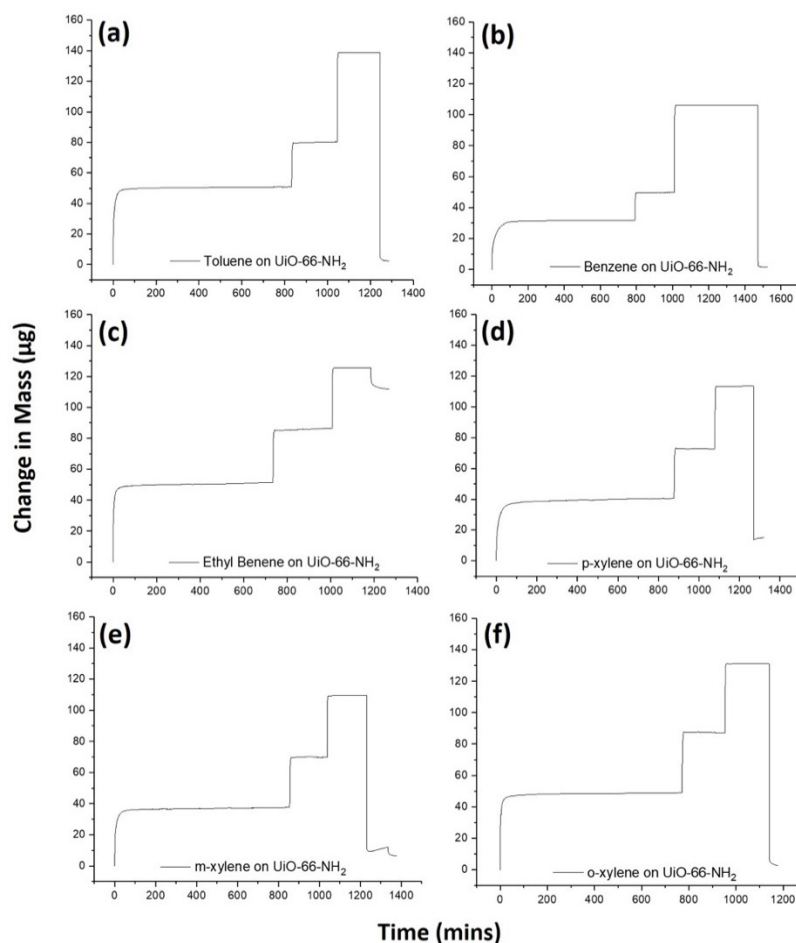


Figure 6. Representative QCM data for adsorption experiments of (a) benzene, (b) toluene, (c) ethylbenzene, (d) *p*-xylene, (e) *m*-xylene, and (f) *o*-xylene on a UiO-66-NH₂ film.

In 2013, Wu et al. used high-resolution powder neutron diffraction to provide the first direct structural evidence for missing linkers in the UiO-66 framework [28]. Ideally, a perfect UiO-66-H framework should have pore volume and surface area of 0.426 cm³/g and 954 m²/g, respectively. If one of twelve linkers are removed, then the pore volume and surface area increase to 0.502 cm³/g and 1433 m²/g, respectively. Several other groups have established the importance of missing linkers in gas adsorption studies in UiO-66 [24–34]. We have calculated the theoretical adsorption capacity (as weight percent) for each MOF assuming one BTEX molecule per pore with no missing linkers. In the ideal UiO-66-X unit cell there are four octahedral pores and eight tetrahedral pores. The Henry's constants can be converted to a weight percent to compare with the theoretical adsorption capacity assuming no defects. From the experimental measurements at 30 °C we find that, on average, there is about one BTEX molecule per unit cell for the UiO-66-H MOF. In the UiO-66-NH₂ MOF, there are about 4–6 BTEX molecules per unit cell, and, within the UiO-66-NO₂ MOFs, there are about 9–11 BTEX molecules per unit cell.

Table 1 shows the measured adsorption capacities in UiO-66-NH₂ and UiO-66-NO₂ films exceed the theoretical adsorption capacity, which suggests that missing linkers are present. The adsorption capacity is calculated for each MOF assuming a defect free and missing-linker structure(s). In the case of the defect free unit cell, we divide the mass of 12 sorbent molecules by the mass of the perfect unit cell. In the case of one missing linker, we divide the mass of 13 sorbent molecules by the mass of the unit cell less one linker, etc. In the case of two missing linkers, we divide the mass of 14 sorbent molecules by the mass of the unit cell less one linker, etc. It can be seen the adsorption capacity for UiO-66-NH₂ and UiO-66-NO₂ is consistent with 1–2 and 3–4 missing linkers, respectively.

Table 1. Measured and calculated adsorption capacity (weight %) for UiO-66-NH₂ and UiO-66-NO₂.

Name	Defect Free	1 Missing Linker	2 Missing Linker	3 Missing Linker	4 Missing Linker	Adsorption Capacity at 20 °C
UiO-66-NH₂						
Benzene	13.50%	15.00%	16.60%	18.20%	20.00%	18.10%
Toluene	15.90%	17.70%	19.60%	21.50%	23.60%	23.20%
Ethyl benzene	18.40%	20.40%	22.60%	24.80%	27.20%	21.10%
<i>p</i> -xylene	18.40%	20.40%	22.60%	24.80%	27.20%	19.20%
<i>m</i> -xylene	18.40%	20.40%	22.60%	24.80%	27.20%	18.10%
<i>o</i> -xylene	18.40%	20.40%	22.60%	24.80%	27.20%	22.00%
UiO-66-NO₂						
Benzene	12.20%	13.60%	15.10%	16.60%	18.30%	21.60%
Toluene	14.40%	16.10%	17.80%	19.60%	21.60%	21.80%
Ethyl benzene	16.60%	18.50%	20.50%	22.60%	24.80%	23.60%
<i>p</i> -xylene	16.60%	18.50%	20.50%	22.60%	24.80%	20.80%
<i>m</i> -xylene	16.60%	18.50%	20.50%	22.60%	24.80%	24.00%
<i>o</i> -xylene	16.60%	18.50%	20.50%	22.60%	24.80%	22.30%

In general, the role of missing linkers in UiO-66 thin films has not been studied in detail. In fact, there are very few reports of UiO-66 films grown directly onto surfaces [35–38]. This is due, in part, to the fact that the common methods for quantifying missing linkers e.g., thermal gravimetric analysis, are not amenable to thin films. To the best of our knowledge, there are only two reports in the literature of UiO-66 films grown on QCM crystals. Virmani et al. measured the adsorption of ethanol at 25 °C into UiO-66-NH₂ films [35]. Semrau et al. measured the adsorption of methanol into UiO-66-H at 40 °C [36]. In the latter study, the authors used X-ray photoelectron spectroscopy to measure the elemental composition of films made using different amounts of a modulator. A comparison of the ideal, defect-free stoichiometry to the measured Zr, C, and O atomic composition can estimate the extent of defects in the films. Semrau et al. reported that films with more defects had an increased adsorption capacity of ethanol.

The role of the functional group is much more difficult to assess experimentally because it is nearly impossible to synthesize ideal materials. Several studies have reported higher adsorption capacity in UiO-66-NH₂ and UiO-66-NO₂ than UiO-66-H [39–45]. In most cases, the smaller pore size of UiO-66-NO₂ and/or UiO-66-NH₂ compared to UiO-66-H is thought to contribute to stronger guest–host interactions. Demir et al. computationally screened 36 functional groups in the UiO-66 framework to assess the relative binding energies for NH₃, H₂O and CO₂. The calculations revealed that the dispersion energy at the UiO-66 pore center was similar for the NH₂ and NO₂ functional groups. In our study, it is most likely that pi–pi interactions between the aromatic molecules and organic linkers dominate the strength of adsorption, as seen in a recent study by Akpınar et al. [46]. Overall, we conclude that the missing linkers play a more important role in our films than the nature of the functional group.

3. Materials and Methods

3.1. UiO-66-X Film Synthesis

UiO-66-H, UiO-66-NH₂, and UiO-66-NO₂ thin films were synthesized using vapor-assisted conversion method previously reported in the literature [35]. All chemicals used were purchased from commercial vendor and used without further purification. A precursor solution was prepared for each respective MOF. The precursor solution for UiO-66-H was prepared by dissolving 9.345 mg (0.0289 mmol) of ZrOCl₂·8H₂O (99.9%, trace metal basis, Bean Town Chemical, Hudson, NY, USA) in 10 mL of dimethylformamide (ACS reagent, ≥99.9%, Sigma Aldrich, St. Louis, MO, USA) by sonication, followed by addition of 6.12 mg (0.03684 mmol) of terephthalic acid (98+%, Alfa Aesar, Haverhill, MA, USA) and 133 µL of glacial acetic acid (JT Baker, Phillipsburg, NJ, USA). The precursor solution

for UiO-66-NH₂ was prepared by dissolving 28.4 mg (0.08813 mmol) of ZrOCl₂·8H₂O (99.9%, trace metal basis, Bean Town Chemical, Hudson, NY, USA) in 10 mL of dimethylformamide (ACS reagent, ≥99.9%, Sigma Aldrich) by sonication, followed by addition of 16.2 mg (0.08943 mmol) of 2-aminoterephthalic acid (99%, Alfa Aesar) and 400 μL of glacial acetic acid (Glacial, JT Baker). The precursor solution for UiO-66-NO₂ was prepared by dissolving 28 mg (0.08689 mmol) of ZrOCl₂·8H₂O (99.9%, trace metal basis, Bean Town Chemical) in 10 mL of dimethylformamide (ACS reagent, ≥99.9%, Sigma Aldrich) by sonication, followed by addition of 18.4 mg (0.08715 mmol) of 2-nitroterephthalic acid (≥99.9%, Sigma Aldrich) and 400 μL of glacial acetic acid (Glacial, JT Baker).

Films were grown onto two types of Au substrates. Planar ~200 nm Au films were grown by vapor deposition onto Cr-primed 15 mm × 15 mm silicon wafers and circular 6 MHz Au-coated quartz microbalance crystals (Inficon part # 750-1057-G10). The substrates were placed on a Teflon o-ring, atop a stainless-steel puck that was placed on the bottom of a 50 mL glass jar. For each synthesis, 50 μL of the respective precursor solution was pipetted onto the Au substrate and a 5 mL aliquot of vapor source solution was then deposited at the bottom of the jar. The vapor source solution was made as a mixture of dimethylformamide (ACS reagent, ≥99.9%, Sigma Aldrich) and acetic acid (Glacial, JT Baker) mixed in a 5.25:1 *v/v* ratio. The vapor source solution was the same for all the reactions. The glass jar was sealed with a Teflon-coated lid and placed in an oven for 3 h at ~100 °C. After 3 h, the sealed jar was removed from the oven and allowed to cool to room temperature.

3.2. X-ray Diffraction

X-ray diffraction spectra were obtained on the films using a Bruker D2 Phaser with Cu Kα radiation (Bruker AXS, Karlsruhe, Germany). Spectra were collected over 5–25° with a 0.24 step size and collected for 12 min.

3.3. Reflection-Infrared Absorption Spectroscopy (RAIRS)

A Bruker Vertex 70 spectrometer (Bruker Scientific, Billerica, MA, USA) was used to collect reflection-absorption infrared spectroscopy (RAIRS) data. The spectrometer was purged with nitrogen gas after 20 min and spectra were collected as an average over 64 scans with a resolution of 4 cm⁻¹.

3.4. Raman Spectroscopy

Raman spectra were collected on a Horiba LabRAM HR800 (Horiba France SAS, Longjumeau, France) using a back-scattering geometry with a 10 X microscope objective. Raman spectra for the UiO-66-H and UiO-66-NO₂ thin films were excited with 532 nm excitation. The scattered radiation was dispersed onto a 1800 groove/mm diffraction grating. The spectra represent the average of 8 scans with a total acquisition time of 30 s per scan. The UiO-66-NH₂ films exhibit photoluminescence with 532 nm excitation so 784 nm excitation was used instead. The scattered radiation was dispersed onto a 950 grooves/mm diffraction grating. The spectra represent the average of 32 scans with a total acquisition time of 15 s per scan.

3.5. Scanning Electron Microscopy (SEM)

SEM images were taken on a JEOL-7000 FE Scanning Electron Microscope and a Thermo Scientific Apreo FE-SEM. Plane-view and cross-sectional SEM images were taken on films grown on the 6 MHz quartz microbalance crystals.

3.6. X-ray Photoelectron Spectroscopy

X-ray photoelectron spectra (Kratos Analytical, Manchester, UK) were taken on a Kratos Axis Ultra DLD using a 45° take-off-angle and 80 eV pass energy. Charge neutralization was used and the C(1s) binding energy was set to 285 eV in each spectrum.

3.7. Gas Doser

In a glovebox (LC Technology Solutions, Salisbury, CMA, USA), the commercially purchased BTEX liquids were transferred into sealed bottles with molecular sieves (3Å) for a minimum of 2 weeks. Approximately 20 mL of each liquid was transferred into a glass ampule fused to a glass-metal joint. The stainless-steel tube was connected to a Nupro valve with Swagelok compression fittings. After the fittings were tightened in the glovebox, the doser was removed and attached to a stainless-steel vacuum chamber. The liquid was subjected to three freeze-pump-thaw cycles to remove the nitrogen gas in the headspace of the ampule.

3.8. Quartz Crystal Microbalance Studies

The MOF-coated 6 MHz QCM crystals were mounted in a high vacuum, stainless steel bakeable sensor (Inficon, Syracuse, NY, USA). The flange was bolted to a stainless-steel vacuum chamber with a conflat flange. The output of the sensor was monitored with an Inficon XTM/2 controller and the crystal frequency was recorded with a home-made Labview program. The MOF film was activated by baking the chamber at ~100 °C for about 12 h under high vacuum. After activation, the chamber was allowed to cool to room temperature. The base pressure of the chamber was less than 1×10^{-7} Torr. The experimental protocol involved stabilizing the crystal temperature initially at 30 °C with an external temperature controller to within ± 0.1 °C. A gate valve between the stainless-steel chamber and turbomolecular pump was closed and the valve to doser was opened. Once the crystal frequency stabilized, the temperature was decreased to 25 °C. The same procedure was repeated down to 20 °C. After the crystal frequency stabilized at 20 °C, the valve to the doser was closed. During the entire experiment, the gas pressure was monitored by a convectron gauge. At the end of data collection, the gate valve to the pump was opened and the residual gas in the chamber was pumped out before starting the bakeout for the next adsorption cycle. At least three adsorption cycles were recorded for each compound on each MOF film. The crystal frequency was converted to a mass using the Sauerbrey equation shown below in Equation (1)

$$\Delta f = -\frac{2f_0^2}{A\sqrt{\rho_q \mu_q}} \Delta m \quad (1)$$

where Δf = change in frequency, f_0 = resonant frequency (6 MHz), A = area of crystal (1.54 cm²), ρ_q = density of quartz (2.649 g/cm³), μ_q = shear modulus of quartz (3.32×10^{11} dyn/cm²), and Δm = change in mass. Specifically, for our 6 MHz crystals the conversion factor is: 20.05 ng/Hz. The Henry's constant, shown in Equation (2), was calculated by dividing the number of moles of adsorbed compound by the product of mass of the MOF thin film (in kg) and pressure of the gas (in Pa). The average values and standard deviation were calculated.

$$K_H = \frac{\text{moles of adsorbate}}{\text{mass of MOF film} \times \text{pressure}} = \frac{\text{mol}}{\text{kg} \cdot \text{Pa}} \quad (2)$$

4. Conclusions

Thin films of the UiO-66-X MOF were synthesized on Au coated QCM crystal surfaces and retained the porosity observed in bulk powders. The UiO-66-H films have the smallest Henry's constant across the BTEX family of compounds at room temperature. This result suggests that the lack of a functional group and larger pore size of UiO-66-H results in weaker adsorbate-adsorbent interactions and, therefore, the smallest Henry's constant. The experimental results suggest that defects strongly influence adsorption capacity. Specifically, the results suggest that the UiO-66-NO₂ films used in this work contain more missing linker defects than the UiO-66-NH₂ films. It was estimated that the UiO-66-NH₂ films have at least two missing linkers per unit cell and the UiO-66-NO₂ films have 3–4 missing linkers per unit cell. In contrast, the greater number of missing linker defects in the UiO-66-NO₂

films effectively increases the pore size, which can accommodate more molecules per unit cell and increase the Henry's constants.

Supplementary Materials: The following are available online at <https://www.mdpi.com/2304-6740/9/1/1/s1>, Figures S1 and S2 show representative adsorption data for the UiO-66-NO₂ and UiO-66-H films, respectively. Table S1 summarizes the Henry's constants measured at 30, 25, and 20 °C.

Author Contributions: Conceptualization, G.S.; methodology, G.S. and J.S.; software, D.S. (Dillon Sinanan) and D.S. (Daniel Speed); validation, J.S., D.S. (Daniel Speed) and G.S.; formal analysis, J.S.; investigation, J.S.; resources, G.S.; data curation, J.S.; writing—original draft preparation, G.S.; writing—review and editing, G.S., J.S., D.S. (Daniel Speed) and D.S. (Dillon Sinanan); visualization, J.S. and D.S. (Daniel Speed); supervision, G.S.; project administration, G.S.; funding acquisition, G.S. All authors have read and agreed to the published version of the manuscript.

Funding: This research was funded in part by the US Department of Education, grant number #P200A150329.

Institutional Review Board Statement: Not applicable.

Informed Consent Statement: Not applicable.

Data Availability Statement: Not applicable.

Acknowledgments: We would like to thank Paul Rupar for access to his glovebox and Michael Buettner for help collecting the X-ray photoelectron spectra.

Conflicts of Interest: The authors declare no conflict of interest.

References

1. Li, H.; Eddaoudi, M.; O'Keeffe, M.; Yaghi, O.M. Design and synthesis of an exceptionally stable and highly porous metal–organic framework. *Nature* **1999**, *402*, 276–279. [[CrossRef](#)]
2. Moghadam, P.Z.; Li, A.; Wiggin, S.B.; Tao, A.; Maloney, A.G.P.; Wood, P.A.; Ward, S.C.; Fairen-Jimenez, D. Development of a Cambridge Structural Database Subset: A Collection of Metal–Organic Frameworks for Past, Present, and Future. *Chem. Mater.* **2017**, *29*, 2618–2625. [[CrossRef](#)]
3. Cavka, J.H.; Jakobsen, S.; Olsbye, U.; Guillou, N.; Lamberti, C.; Bordiga, S.; Lillerud, K.P. A New Zirconium Inorganic Building Brick Forming Metal Organic Frameworks with Exceptional Stability. *J. Am. Chem. Soc.* **2008**, *130*, 13850–13851. [[CrossRef](#)] [[PubMed](#)]
4. Kandiah, M.; Nilsen, M.H.; Usseglio, S.; Jakobsen, S.; Olsbye, U.; Tilset, M.; Larabi, C.; Quadrelli, E.A.; Bonino, F.; Lillerud, K.P. Synthesis and Stability of Tagged UiO-66 Zr-MOFs. *Chem. Mater.* **2010**, *22*, 6632–6640. [[CrossRef](#)]
5. Shearer, G.C.; Forselv, S.; Chavan, S.; Bordiga, S.; Mathisen, K.; Bjørgen, M.; Svelle, S.; Lillerud, K.P. In Situ Infrared Spectroscopic and Gravimetric Characterisation of the Solvent Removal and Dehydroxylation of the Metal Organic Frameworks UiO-66 and UiO-67. *Top. Catal.* **2013**, *56*, 770–782. [[CrossRef](#)]
6. DeCoste, J.B.; Peterson, G.W.; Jasuja, H.; Glover, T.G.; Huang, Y.-G.; Walton, K.S. Stability and degradation mechanisms of metal–organic frameworks containing the Zr₆O₄(OH)₄ secondary building unit. *J. Mater. Chem. A* **2013**, *1*, 5642–5650. [[CrossRef](#)]
7. Valenzano, L.; Civalieri, B.; Chavan, S.; Bordiga, S.; Nilsen, M.H.; Jakobsen, S.; Lillerud, K.P.; Lamberti, C. Disclosing the Complex Structure of UiO-66 Metal Organic Framework: A Synergic Combination of Experiment and Theory. *Chem. Mater.* **2011**, *23*, 1700–1718. [[CrossRef](#)]
8. Øien, S.; Wragg, D.; Reinsch, H.; Svelle, S.; Bordiga, S.; Lamberti, C.; Lillerud, K.P. Detailed Structure Analysis of Atomic Positions and Defects in Zirconium Metal–Organic Frameworks. *Cryst. Growth Des.* **2014**, *14*, 5370–5372. [[CrossRef](#)]
9. Lennox, M.J.; Düren, T. Understanding the Kinetic and Thermodynamic Origins of Xylene Separation in UiO-66(Zr) via Molecular Simulation. *J. Phys. Chem. C* **2016**, *120*, 18651–18658. [[CrossRef](#)]
10. Finsy, V.; Verelst, H.; Alaerts, L.; De Vos, D.; Jacobs, P.A.; Baron, G.V.; Denayer, J.F.M. Pore-Filling-Dependent Selectivity Effects in the Vapor-Phase Separation of Xylene Isomers on the Metal–Organic Framework MIL-47. *J. Am. Chem. Soc.* **2008**, *130*, 7110–7118. [[CrossRef](#)]
11. Gu, Z.-Y.; Jiang, D.-Q.; Wang, H.-F.; Cui, X.-Y.; Yan, X.-P. Adsorption and Separation of Xylene Isomers and Ethylbenzene on Two Zn–Terephthalate Metal–Organic Frameworks. *J. Phys. Chem. C* **2010**, *114*, 311–316. [[CrossRef](#)]
12. Rives, S.; Jobic, H.; Kolokolov, D.I.; Gabrienko, A.A.; Stepanov, A.G.; Ke, Y.; Frick, B.; Devic, T.; Férey, G.; Maurin, G. Diffusion of Xylene Isomers in the MIL-47(V) MOF Material: A Synergic Combination of Computational and Experimental Tools. *J. Phys. Chem. C* **2013**, *117*, 6293–6302. [[CrossRef](#)]
13. Peralta, D.; Chaplais, G.; Paillaud, J.-L.; Simon-Masseron, A.; Barthelet, K.; Pirngruber, G.D. The separation of xylene isomers by ZIF-8: A demonstration of the extraordinary flexibility of the ZIF-8 framework. *Microporous Mesoporous Mater.* **2013**, *173*, 1–5. [[CrossRef](#)]

14. Duerinck, T.; Bueno-Perez, R.; Vermoortele, F.; De Vos, D.E.; Calero, S.; Baron, G.V.; Denayer, J.F.M. Understanding Hydrocarbon Adsorption in the UiO-66 Metal–Organic Framework: Separation of (Un) saturated Linear, Branched, Cyclic Adsorbates, Including Stereoisomers. *J. Phys. Chem. C* **2013**, *117*, 12567–12578. [[CrossRef](#)]
15. Ramsahye, N.A.; Gao, J.; Jobic, H.; Llewellyn, P.L.; Yang, Q.; Wiersum, A.D.; Koza, M.M.; Guillermin, V.; Serre, C.; Zhong, C.L.; et al. Adsorption and Diffusion of Light Hydrocarbons in UiO-66(Zr): A Combination of Experimental and Modeling Tools. *J. Phys. Chem. C* **2014**, *118*, 27470–27482. [[CrossRef](#)]
16. Trens, P.; Belarbi, H.; Shepherd, C.; Gonzalez, P.; Ramsahye, N.A.; Lee, U.H.; Seo, Y.-K.; Chang, J.-S. Adsorption and separation of xylene isomers vapors onto the chromium terephthalate-based porous material MIL-101(Cr): An experimental and computational study. *Microporous Mesoporous Mater.* **2014**, *183*, 17–22. [[CrossRef](#)]
17. Gonzalez, M.I.; Kapelewski, M.T.; Bloch, E.D.; Milner, P.J.; Reed, D.A.; Hudson, M.R.; Mason, J.A.; Barin, G.; Brown, C.M.; Long, J.R. Separation of Xylene Isomers through Multiple Metal Site Interactions in Metal–Organic Frameworks. *J. Am. Chem. Soc.* **2018**, *140*, 3412–3422. [[CrossRef](#)]
18. Grissom, T.G.; Sharp, C.H.; Usov, P.M.; Troya, D.; Morris, A.J.; Morris, J.R. Benzene, Toluene, and Xylene Transport through UiO-66: Diffusion Rates, Energetics, and the Role of Hydrogen Bonding. *J. Phys. Chem. C* **2018**, *122*, 16060–16069. [[CrossRef](#)]
19. Driscoll, D.M.; Troya, D.; Usov, P.M.; Maynes, A.J.; Morris, A.J.; Morris, J.R. Characterization of Undercoordinated Zr Defect Sites in UiO-66 with Vibrational Spectroscopy of Adsorbed CO. *J. Phys. Chem. C* **2018**, *122*, 14582–14589. [[CrossRef](#)]
20. Cui, W.-G.; Hu, T.-L.; Bu, X.-H. Metal–Organic Framework Materials for the Separation and Purification of Light Hydrocarbons. *Adv. Mater.* **2020**, *32*, 1806445. [[CrossRef](#)]
21. Barcia, P.S.; Guimaraes, D.; Mendes, P.A.P.; Silva, J.A.C.; Guillermin, V.; Chevreau, H.; Serre, C.; Rodrigues, A.E. Reverse shape selectivity in the adsorption of hexane and xylene isomers in MOF UiO-66. *Microporous Mesoporous Mater.* **2011**, *139*, 67–73. [[CrossRef](#)]
22. Chang, N.; Yan, X.-P. Exploring reverse shape selectivity and molecular sieving effect of metal–organic framework UiO-66 coated capillary column for gas chromatographic separation. *J. Chromatogr. A* **2012**, *1257*, 116–124. [[CrossRef](#)] [[PubMed](#)]
23. Granato, M.A.; Martins, V.D.; Ferreira, A.F.P.; Rodrigues, A.E. Adsorption of xylene isomers in MOF UiO-66 by molecular simulation. *Microporous Mesoporous Mater.* **2014**, *190*, 165–170. [[CrossRef](#)]
24. Katz, M.J.; Brown, Z.J.; Colon, Y.J.; Siu, P.W.; Scheidt, K.A.; Snurr, R.Q.; Hupp, J.T.; Farha, O.K. A facile synthesis of UiO-66, UiO-67 and their derivatives. *Chem. Commun.* **2013**, *49*, 9449–9451. [[CrossRef](#)] [[PubMed](#)]
25. Shearer, G.C.; Chavan, S.; Bordiga, S.; Svelle, S.; Olsbye, U.; Lillerud, K.P. Defect Engineering: Tuning the Porosity and Composition of the Metal–Organic Framework UiO-66 via Modulated Synthesis. *Chem. Mater.* **2016**, *28*, 3749–3761. [[CrossRef](#)]
26. Morris, W.; Wang, S.; Cho, D.; Auyeung, E.; Li, P.; Farha, O.K.; Mirkin, C.A. Role of Modulators in Controlling the Colloidal Stability and Polydispersity of the UiO-66 metal–Organic framework. *ACS Appl. Mater. Interfaces* **2017**, *9*, 33413–33418. [[CrossRef](#)]
27. Atzori, C.; Shearer, G.C.; Maschio, L.; Civalieri, B.; Bonino, F.; Lamberti, C.; Svelle, S.; Lillerud, K.P.; Bordiga, S. Effect of Benzoic Acid as a Modulator in the Structure of UiO-66: An Experimental and Computational Study. *J. Phys. Chem. C* **2017**, *121*, 9312–9324. [[CrossRef](#)]
28. Wu, H.; Chua, Y.S.; Krungleviciute, V.; Tyagi, M.; Chen, P.; Yildirim, T.; Zhou, W. Unusual and Highly Tunable Missing-Linker Defects in Zirconium Metal–Organic Framework UiO-66 and Their Important Effects on Gas Adsorption. *J. Am. Chem. Soc.* **2013**, *135*, 10525–10532. [[CrossRef](#)]
29. Cliffe, M.J.; Wan, W.; Zou, X.; Chater, P.A.; Kleppe, A.K.; Tucker, M.G.; Wilhelm, H.; Funnell, N.P.; Coudert, F.-X.; Goodwin, A.L. Correlated defect nanoregions in a metal–organic framework. *Nat. Commun.* **2014**, *5*, 4176. [[CrossRef](#)]
30. Shearer, G.C.; Chavan, S.; Ethiraj, J.; Vitillo, J.G.; Svelle, S.; Olsbye, U.; Lamberti, C.; Bordiga, S.; Lillerud, K.P. Tuned to Perfection: Ironing Out the Defects in Metal–Organic Framework UiO-66. *Chem. Mater.* **2014**, *26*, 4068–4071. [[CrossRef](#)]
31. Vandichel, M.; Hajek, J.; Vermoortele, F.; Waroquier, M.; De Vos, D.E.; Van Speybroeck, V. Active site engineering in UiO-66 type metal–organic frameworks by intentional creation of defects: A theoretical rationalization. *CrystEngComm* **2015**, *17*, 395–406. [[CrossRef](#)]
32. Liang, W.; Coghlan, C.J.; Ragon, F.; Rubio-Martinez, M.; D’Alessandro, D.M.; Babarao, R. Defect engineering of UiO-66 for CO₂ and H₂O uptake—A combined experimental and simulation study. *Dalton Trans.* **2016**, *45*, 4496–4500. [[CrossRef](#)] [[PubMed](#)]
33. Idrees, K.B.; Chen, Z.; Zhang, X.; Mian, M.R.; Drout, R.J.; Islamoglu, T.; Farha, O.K. Tailoring Pore Aperture and Structural Defects in Zirconium-Based Metal–Organic Frameworks for Krypton/Xenon Separation. *Chem. Mater.* **2020**, *32*, 3776–3782. [[CrossRef](#)]
34. Winarta, J.; Shan, B.; McIntyre, S.M.; Ye, L.; Wang, C.; Liu, J.; Mu, B. A Decade of UiO-66 Research: A Historic Review of Dynamic Structure, Synthesis Mechanisms, and Characterization Techniques of an Archetypal Metal–Organic Framework. *Cryst. Growth Des.* **2020**, *20*, 1347–1362. [[CrossRef](#)]
35. Virmani, E.; Rotter, J.M.; Mahringer, A.; von Zons, T.; Godt, A.; Bein, T.; Wuttke, S.; Medina, D.D. On-Surface Synthesis of Highly Oriented Thin Metal–Organic Framework Films through Vapor-Assisted Conversion. *J. Am. Chem. Soc.* **2018**, *140*, 4812–4819. [[CrossRef](#)]
36. Semrau, A.L.; Wannapaiboon, S.; Pujari, S.P.; Vervoorts, P.; Albada, B.; Zuillhof, H.; Fischer, R.A. Highly Porous Nanocrystalline UiO-66 Thin Films via Coordination Modulation Controlled Step-by-Step Liquid-Phase Growth. *Cryst. Growth Des.* **2019**, *19*, 1738–1747. [[CrossRef](#)]
37. Miyamoto, M.; Kohmura, S.; Iwatsuka, H.; Oumi, Y.; Uemiyama, S. In situ solvothermal growth of highly oriented Zr-based metal organic framework UiO-66 film with monocrystalline layer. *CrystEngComm* **2015**, *17*, 3422–3425. [[CrossRef](#)]

38. Hashem, T.; Valdez Sanchez, E.P.; Weidler, P.; Gliemann, H.; Alkordi, M.H.; Wöll, C. Liquid-Phase Quasi-Epitaxial Growth of Highly Stable, Monolithic UiO-66-NH₂ MOF thin Films on Solid Surfaces. *ChemistryOpen* **2020**, *9*, 524–527. [[CrossRef](#)]
39. Cmarik, G.E.; Kim, M.; Cohen, S.M.; Walton, K.S. Tuning the Adsorption Properties of UiO-66 via Ligand Functionalization. *Langmuir* **2012**, *28*, 15606–15613. [[CrossRef](#)]
40. Jasuja, H.; Peterson, G.W.; Decoste, J.B.; Browe, M.A.; Walton, K.S. Evaluation of MOFs for air purification and air quality control applications: Ammonia removal from air. *Chem. Eng. Sci.* **2015**, *124*, 118–124. [[CrossRef](#)]
41. DeCoste, J.B.; Browe, M.A.; Wagner, G.W.; Rossin, J.A.; Peterson, G.W. Removal of chlorine gas by an amine functionalized metal–organic framework via electrophilic aromatic substitution. *Chem. Commun.* **2015**, *51*, 12474–12477. [[CrossRef](#)] [[PubMed](#)]
42. Peterson, G.W.; DeCoste, J.B.; Fatollahi-Fard, F.; Britt, D.K. Engineering UiO-66-NH₂ for Toxic Gas Removal. *Ind. Eng. Chem. Res.* **2014**, *53*, 701–707. [[CrossRef](#)]
43. Rada, Z.H.; Abid, H.R.; Sun, H.; Shang, J.; Li, J.; He, Y.; Liu, S.; Wang, S. Effects of –NO₂ and –NH₂ functional groups in mixed-linker Zr-based MOFs on gas adsorption of CO₂ and CH₄. *Prog. Nat. Sci. Mater. Int.* **2018**, *28*, 160–167. [[CrossRef](#)]
44. Vellingiri, K.; Kumar, P.; Deep, A.; Kim, K.-H. Metal–organic frameworks for the adsorption of gaseous toluene under ambient temperature and pressure. *Chem. Eng. J.* **2017**, *307*, 1116–1126. [[CrossRef](#)]
45. Demir, H.; Walton, K.S.; Sholl, D.S. Computational Screening of Functionalized UiO-66 Materials for Selective Contaminant Removal from Air. *J. Phys. Chem. C* **2017**, *121*, 20396–20406. [[CrossRef](#)]
46. Akpınar, I.; Drout, R.J.; Isamoglu, T.; Kato, S.; Lyu, J.; Farha, O.K. Exploiting π – π interactions to design an efficient sorbent for atrazine removal from water. *ACS Appl. Mater. Interfaces* **2019**, *11*, 6097–6103. [[CrossRef](#)]